
This is an electronic reprint of the original article.
This reprint may differ from the original in pagination and typographic detail.

Kwon, Do Hoon; Tretyakov, Sergei

Perfect reflection control for impenetrable surfaces using surface waves of orthogonal polarization

Published in:
Physical Review B

DOI:
[10.1103/PhysRevB.96.085438](https://doi.org/10.1103/PhysRevB.96.085438)

Published: 28/08/2017

Document Version
Publisher's PDF, also known as Version of record

Please cite the original version:
Kwon, D. H., & Tretyakov, S. A. (2017). Perfect reflection control for impenetrable surfaces using surface waves of orthogonal polarization. *Physical Review B*, 96(8), [085438]. DOI: 10.1103/PhysRevB.96.085438

This material is protected by copyright and other intellectual property rights, and duplication or sale of all or part of any of the repository collections is not permitted, except that material may be duplicated by you for your research use or educational purposes in electronic or print form. You must obtain permission for any other use. Electronic or print copies may not be offered, whether for sale or otherwise to anyone who is not an authorised user.

Perfect reflection control for impenetrable surfaces using surface waves of orthogonal polarizationDo-Hoon Kwon^{1,2,*} and Sergei A. Tretyakov²¹*Department of Electrical and Computer Engineering, University of Massachusetts Amherst, Amherst, Massachusetts 01003, USA*²*Department of Electronics and Nanoengineering, Aalto University, P.O. Box 15500, 00076 Aalto, Finland*

(Received 26 April 2017; revised manuscript received 28 July 2017; published 28 August 2017)

For impenetrable electromagnetic surfaces, a metasurface design approach for perfect control of the reflection phenomena using gradient anisotropic tensor surface impedance is presented. It utilizes a set of orthogonally polarized auxiliary surface waves to create pointwise reactive impedance characteristics by channeling power along the tangential direction of the surface in the near zone in a carefully designed manner. The propagating incident and reflected fields do not interfere with the surface waves due to the polarization orthogonality. Design examples of an anomalous reflector and a power splitter for an incident plane wave are presented and numerically verified. Realization possibilities using an array of rotated metallic resonators on a thin grounded dielectric substrate are discussed.

DOI: [10.1103/PhysRevB.96.085438](https://doi.org/10.1103/PhysRevB.96.085438)**I. INTRODUCTION**

As electrically thin engineered composite layers, metasurfaces show the promise of overcoming the high level of loss typically associated with traditional volumetric metamaterials, which is the main challenge in their adoption in practical applications. Similar to their volumetric counterparts, electromagnetic metasurfaces offer a host of novel possibilities of controlling and synthesizing electromagnetic wave propagation, reflection, and scattering phenomena [1–4]. Spatially uniform metasurfaces are able to perform traditional functions such as perfect absorption [5,6], reflection with an arbitrary phase [7], and polarization transformation [8] with subwavelength-thin layers. Furthermore, gradient metasurfaces having spatially inhomogeneous surface parameters have been recently shown to realize anomalous reflection and refraction [9–12], near- and far-zone focusing [13–15], holograms [16–18], etc.

Most gradient metasurface designs are based on the idea of imparting a position-dependent custom phase to the transmitted or reflected wave front, which has been recently formalized as the generalized law of reflection and refraction [9]. Toward ideal anomalous reflection or refraction properties, the magnitude of the local reflection or transmission coefficients is maximized in the design process. One effective approach in a transmissive application is employing an array of resonant particles for inducing a balanced combination of electric and magnetic polarization currents by the incident field with a linear phase gradient in space, as was demonstrated in the low-reflection beam refraction using a Huygens metasurface [19]. For reflective applications, linear modulation of the reflection phase for deflecting an incident wave upon reflection according to the generalized law of reflection has been widely used in the theory and practice of reflectarray antennas [20].

Recent theoretical studies have revealed that anomalous reflection and refraction of plane waves based on the generalized Snell's law [9] can never be perfect in the power-conversion efficiency and necessarily entail propagating diffraction orders or Floquet-mode harmonics into undesired directions [21,22].

For perfect anomalous reflection or refraction, the wave impedance of the reflected or refracted plane wave is different from that of the incident plane wave. As a result, the required magnitude of the reflection or transmission coefficient deviates from unity, conflicting with the assumption behind the generalized Snell's law for lossless metasurfaces. By specifying the incident and scattered (reflected or transmitted) fields under the power-conservation condition, the required surface parameter distribution can be derived. For perfect refraction of a plane wave, it is found that a homogeneous Ω -type bianisotropic surface [7,23] can perform the transformation. For perfect anomalous reflection, the metasurface specification associated with an incident plane wave and a power-conserved reflected plane wave turns out to be strongly nonlocal, exhibiting alternating active and lossy spatial ranges [21,22], while the metasurface remains lossless over a wavelength scale. Hence, it is concluded that the metasurface must accept the incident power over the “lossy” range and channel it along the surface before releasing it over the “active” range. In [12], the leaky-wave antenna principle was applied to design and optimize a supercell comprising an array of conductor strips to realize the nonlocal reflection properties. In [24], an auxiliary set of surface waves was introduced in addition to the incident and scattered plane waves to derive a passive, lossless Ω -type bianisotropic metasurface for perfect wave transformation. Surface waves were added to the illuminated side in the beam-splitter design; they were added in the shadow side in the beam-reflector design. In order to obtain perfect reflection on a shielded surface, a set of propagating waves was added as the auxiliary fields between an Ω metasurface and the perfect electric conductor (PEC) surface [25]. In this Ω -metasurface design approach, the side of the metasurface for surface-wave introduction and the exact surface-wave specification are available for design choices. The technique is suitable for penetrable metasurfaces.

In this paper, a design recipe for impenetrable metasurfaces in terms of the anisotropic tensor surface impedance is presented for perfect plane-wave reflection transformations. Building on the approach introduced in [24,25], surface waves are introduced to avoid a nonlocal, active-lossy profile and obtain pointwise lossless characteristics. The key difference is that the surface waves are polarized orthogonal to the

*dhkwon@umass.edu

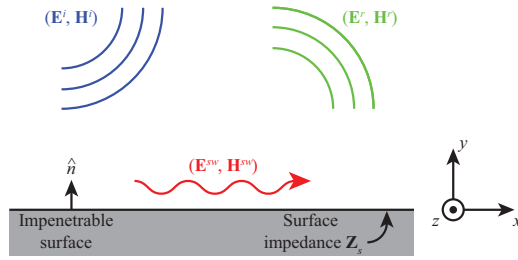


FIG. 1. General reflection transformation by a planar impenetrable surface modeled with a surface-impedance tensor \mathbf{Z}_s .

incident and reflected fields so that the two sets of fields do not interfere. The total fields are confined to the illuminated side of the metasurface, allowing an ultrathin physical design for reflective structures, characterized by a surface impedance. In contrast, a transmissive surface, described by a transition condition, is needed even for reflection applications with Ω -bianisotropic metasurfaces [24,25]. As design examples, a reflecting surface for perfect 0° -to- 70° anomalous reflection [12] and a plane-wave splitter with an unequal 1:9 power division are presented. In the leaky-wave approach [12], the power-channeling evanescent waves, which are copolarized, could not be analytically quantified to characterize the reflecting surface. The leaky-wave principle was used as a design guide, and numerical optimization was used for fine tuning. In this study, exploiting an orthogonal polarization for the surface waves allows a closed-form characterization of the surface at the expense of an increased realization complexity due to the tensorial nature of the surface impedance. A design specification is given in terms of a position-dependent anisotropic tensor surface impedance. A tensor surface impedance may be realized using a rotated array of resonant particles over a conductor surface, such as an array of rectangular patches on a grounded dielectric substrate. With all the fields limited to the illuminated side of the metasurface, the proposed approach gives design recipes for electrically thin designs suitable for shielded or impenetrable mounting platforms.

II. SURFACE-IMPEDANCE CHARACTERIZATION OF GENERAL REFLECTION TRANSFORMATION

A general reflection transformation by an impenetrable surface is illustrated in Fig. 1. At an angular frequency ω , let the time-harmonic incident electric and magnetic fields characterized by phasors $(\mathbf{E}^i, \mathbf{H}^i)$ illuminate an electromagnetically impenetrable surface at $y = 0$. It is desired that the surface impedance \mathbf{Z}_s be designed such that the reflected fields have some predefined, desirable properties characterized by $(\mathbf{E}^r, \mathbf{H}^r)$. In transforming $(\mathbf{E}^i, \mathbf{H}^i)$ into $(\mathbf{E}^r, \mathbf{H}^r)$ upon reflection, an auxiliary set of surface-wave fields $(\mathbf{E}^{sw}, \mathbf{H}^{sw})$ may be introduced to allow flexibility into the properties of \mathbf{Z}_s and its potential implementation as a metasurface. Each of the three field pairs satisfies Maxwell's equations individually and exists only in the incident medium, which is assumed to be free space.

The total fields (\mathbf{E}, \mathbf{H}) in $y \geq 0$ are given by superposition as

$$\mathbf{E} = \mathbf{E}^i + \mathbf{E}^r + \mathbf{E}^{sw}, \quad \mathbf{H} = \mathbf{H}^i + \mathbf{H}^r + \mathbf{H}^{sw}. \quad (1)$$

On the reflector surface, let the tangential field vectors be denoted by $(\mathbf{E}_t, \mathbf{H}_t)$ and given by

$$\mathbf{E}_t = \mathbf{E}(y=0) - \hat{n}[\hat{n} \cdot \mathbf{E}(y=0)], \quad (2)$$

$$\mathbf{H}_t = \mathbf{H}(y=0) - \hat{n}[\hat{n} \cdot \mathbf{H}(y=0)], \quad (3)$$

where $\hat{n} = \hat{y}$. A general case allows the existence of both a surface electric current $\mathbf{J}_s = \hat{n} \times \mathbf{H}_t$ and a magnetic current $\mathbf{M}_s = \mathbf{E}_t \times \hat{n}$. The surface impedance \mathbf{Z}_s relates the electric surface current and the tangential electric field via

$$\mathbf{E}_t = \mathbf{Z}_s \mathbf{J}_s = \mathbf{Z}_s \hat{n} \times \mathbf{H}_t. \quad (4)$$

Here, \mathbf{Z}_s can be written as a 2×2 matrix in the xz plane with four independent complex-valued entries in the most general case, where active and/or nonreciprocal surface properties are permitted. Since there are only two equations in (4), the surface impedance \mathbf{Z}_s that can support the given tangential field pair $(\mathbf{E}_t, \mathbf{H}_t)$ on the reflector surface is not unique.

Let us consider \mathbf{Z}_s of the form

$$\mathbf{Z}_s = j\mathbf{X}_s = j \begin{bmatrix} X_{xx} & X_{xz} \\ X_{zx} & X_{zz} \end{bmatrix}, \quad (5)$$

where the four reactance elements are real valued. In an isotropic case, \mathbf{X}_s reduces to a scalar, corresponding to a lossless reactive surface. When $X_{xz} = X_{zx}$, the reactance tensor represents a reciprocal surface. With four arbitrary element values, it is noted that (5) still permits active or nonreciprocal properties. With a decomposition of tangential fields as $\mathbf{E}_t = \hat{x}E_{tx} + \hat{z}E_{tz}$ and $\mathbf{H}_t = \hat{x}H_{tx} + \hat{z}H_{tz}$, (4) can be written in a matrix form as

$$\begin{bmatrix} E_{tx} \\ E_{tz} \end{bmatrix} = j \begin{bmatrix} X_{xx} & X_{xz} \\ X_{zx} & X_{zz} \end{bmatrix} \begin{bmatrix} H_{tx} \\ -H_{tz} \end{bmatrix}. \quad (6)$$

Equating both the real and imaginary parts on the two sides of (6), the reactance tensor is uniquely determined to be

$$\mathbf{X}_s = \frac{1}{\text{Im}\{H_{tx}H_{tz}^*\}} \begin{bmatrix} \text{Re}\{E_{tx}H_{tx}^*\} & \text{Re}\{E_{tx}H_{tz}^*\} \\ \text{Re}\{E_{tz}H_{tx}^*\} & \text{Re}\{E_{tz}H_{tz}^*\} \end{bmatrix}. \quad (7)$$

The same boundary may be characterized in terms of the surface admittance tensor $\mathbf{Y}_s = \mathbf{Z}_s^{-1} = j\mathbf{B}_s = -j\mathbf{X}_s^{-1}$, where the surface susceptance tensor \mathbf{B}_s is expressed as

$$\mathbf{B}_s = \frac{1}{\text{Im}\{E_{tx}E_{tz}^*\}} \begin{bmatrix} -\text{Re}\{E_{tz}H_{tz}^*\} & \text{Re}\{E_{tx}H_{tz}^*\} \\ \text{Re}\{E_{tz}H_{tx}^*\} & -\text{Re}\{E_{tx}H_{tx}^*\} \end{bmatrix}. \quad (8)$$

For the assumed form of \mathbf{Z}_s in (5), a lossless, reciprocal surface results when the off-diagonal elements of (7) and (8) are equal to each other. We recognize that this condition is equivalent to

$$S_n = \hat{y} \cdot \frac{1}{2} \text{Re}\{\mathbf{E}_t \times \mathbf{H}_t^*\} = 0, \quad (9)$$

where S_n is the normal component of the time-average Poynting vector on the reflector surface. At a given point $(x, 0, z)$ on the reflecting surface, the surface is locally lossless and reciprocal if there is no net power flow through the boundary at that point. This is analogous to the local power-conservation condition considered in the Ω -bianisotropic metasurface design [23]. For a desired far-zone reflection transformation specified by $(\mathbf{E}^i, \mathbf{H}^i)$ and $(\mathbf{E}^r, \mathbf{H}^r)$, one obtains a lossless, reciprocal, and anisotropic surface-impedance

specification if (9) can be satisfied globally by introducing proper surface-wave fields ($\mathbf{E}^{sw}, \mathbf{H}^{sw}$).

Derivation of the surface-impedance parameters indicates that the total fields (1) must satisfy (7) or (8) on the impenetrable surface. Conversely, the surface impedance \mathbf{Z}_s can be regarded as a generator for the induced surface currents \mathbf{J}_s and \mathbf{M}_s for creating the proper set of scattered fields, i.e., $(\mathbf{E}^s, \mathbf{H}^s) = (\mathbf{E}^r + \mathbf{E}^{sw}, \mathbf{H}^r + \mathbf{H}^{sw})$, when a given set of incident fields ($\mathbf{E}^i, \mathbf{H}^i$) illuminates the surface. Here, it should be remembered that this reverse relation holds as long as the surface parameters are either lossy or lossless, taken as the limiting case of vanishing loss, according to the uniqueness theorem [26]. If the reflecting surface includes an active region, the scattered fields generated by the secondary sources on the surface may contain additional fields associated with the excitation-free solutions to the overall configuration, which is undesirable from a design perspective.

III. THREE-CHANNEL PLANE-WAVE REFLECTION CONTROLLER USING PERIODIC IMPEDANCE SURFACES

The design of surface impedance for synthesizing an envisioned, custom reflection property in Sec. II is applicable to any combination of propagating and evanescent fields for the incident and reflected fields. Toward applying the technique to practical applications, plane-wave reflection control enabled by *periodic* impedance surfaces is considered in this section.

Custom plane-wave reflection by a planar surface can be formulated in the multichannel reflector paradigm [27]. As an example, a general three-channel plane-wave reflector is illustrated in Fig. 2(a). For a given angle of incidence θ^i and a period D_x for the surface impedance, the x wave number of the m th reflected Floquet harmonic is given by

$$k_{xm}^r = k \sin \theta^i + \frac{2m\pi}{D_x}, \quad (10)$$

where k is the free-space wave number. For the three reflected propagating modes ($m = -1, 0, 1$), the angle of reflection θ_m^r is found from $k_{xm}^r = k \sin \theta_m^r$ [28]. The reflected fields ($\mathbf{E}^r, \mathbf{H}^r$) can be specified by a superposition of plane waves propagating in these three directions, as desired, under the condition of power conservation. Then, surface-wave fields are carefully chosen and added to the incident and reflected fields in order for the total fields to satisfy (9). Finally, the required surface-impedance parameters are found from (7) and (8).

As a concrete design example of a three-channel reflection controller, an anomalous reflection-controller surface design exhibiting lossless, reciprocal surface parameters is presented. Figure 2(b) illustrates a TE-polarized plane wave (to the surface normal \hat{y} direction) illuminating a reflecting surface in the xz plane at normal incidence. It is desired that the incident power is split between two propagating reflected plane waves making angles $\pm\theta^r$ with the $+y$ axis (measured in the clockwise direction), without any back-reflected plane wave propagating in the $+\hat{y}$ direction. Three port numbers according to the multichannel functional metasurface [27] are also indicated in Fig. 2(b).

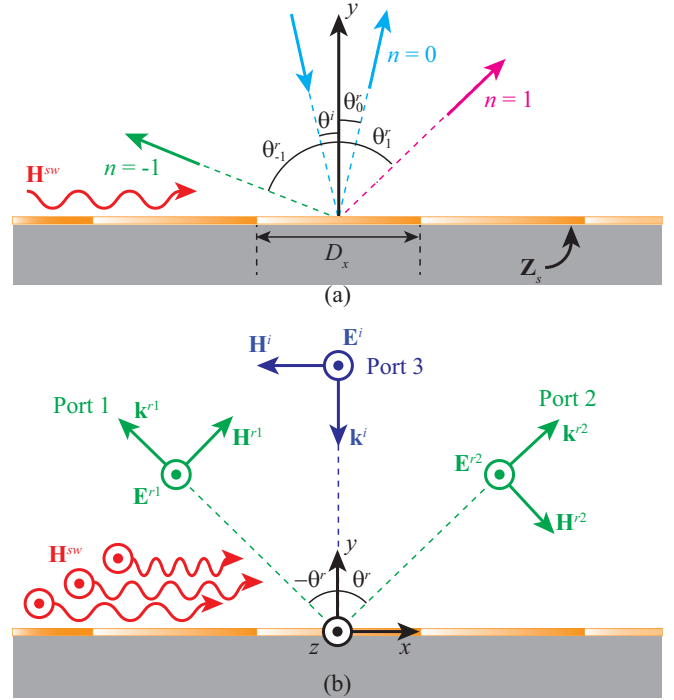


FIG. 2. Three-channel flat plane-wave reflection controller using a periodic impedance surface. (a) Three propagating channels defined by the angle of incidence and the propagating Floquet mode index n . The period of the surface-impedance parameters is D_x . (b) A three-channel reflecting surface illuminated by a normally incident plane wave of TE polarization. A set of TM-polarized surface waves are introduced to obtain pointwise lossless, reactive surface-impedance characteristics. Three plane-wave port designations are also shown.

Using an $e^{j\omega t}$ time convention assumed and suppressed, let the electric fields of the incident and reflected plane waves be written as

$$\mathbf{E}^i = \hat{z} E_0^i e^{jk_y y}, \quad (11)$$

$$\mathbf{E}^{r1} = \hat{z} E_0^{r1} e^{-j(k_x^r x + k_y^r y)}, \quad (12)$$

$$\mathbf{E}^{r2} = \hat{z} E_0^{r2} e^{-j(k_x^r x + k_y^r y)}, \quad (13)$$

where $E_0^i, E_0^{r1}, E_0^{r2}$ are E -field amplitudes, $k_x^r = k \sin \theta^r$, and $k_y^r = k \cos \theta^r$. The associated H fields, $\mathbf{H}^i, \mathbf{H}^{r1}$, and \mathbf{H}^{r2} , are found from the standard plane-wave relationship with the E fields. For a power-conserving split, the three field amplitudes are related by

$$\frac{|E_0^i|^2}{Z_i} = \frac{|E_0^{r1}|^2 + |E_0^{r2}|^2}{Z_r}, \quad (14)$$

where $Z_i = \eta$ and $Z_r = \eta / \cos \theta^r$ ($\eta \approx 377\Omega$ is the free-space intrinsic impedance) are the wave impedances in the xz plane for the incident and two reflected plane waves, respectively. The superposition of the incident and reflected fields is periodic in x with a period given by

$$D_x = \frac{2\pi}{k_x^r} = \frac{\lambda}{\sin \theta^r}, \quad (15)$$

where λ is the free-space wavelength.

Let the reflected E -field amplitudes be defined relative to the incident E -field amplitude as

$$E_0^{r1} = a_1 e^{j\delta_1} E_0^i, \quad E_0^{r2} = a_2 e^{j\delta_2} E_0^i, \quad (16)$$

where a_1, a_2 and δ_1, δ_2 are relative magnitudes and phases of E_0^{r1}, E_0^{r2} with respect to those of E_0^i . For this TE-mode set of fields, the normal component of the Poynting vector on the surface is expressed as

$$S_n^{\text{TE}} = -\frac{|E_0^i|^2}{2} \left(\frac{1}{Z_i} - \frac{1}{Z_r} \right) a \cos(k_x^r x + \delta) + \frac{a_1 a_2 |E_0^i|^2}{Z_r} \cos(2k_x^r x - \delta_2 + \delta_1), \quad (17)$$

where a and δ are the magnitude and phase of the complex number

$$a e^{j\delta} = (a_1 \cos \delta_1 + a_2 \cos \delta_2) + j(a_1 \sin \delta_1 - a_2 \sin \delta_2). \quad (18)$$

We find that (17) is a periodic function with a period of $\pi/k \sin \theta^r$, created by interference between the three propagating waves in (11)–(13). The first term in (17) vanishes for an equal-power split ($a_1 = a_2$) combined with a specific phase relation between the two reflected fields ($\delta_1 + \delta_2 = \pi$). The second term vanishes if one of the two reflected plane waves is not present, i.e., when all the incident power is reflected into one off-normal direction. With respect to x , S_n alternates between positive and negative values. Hence, if the set of three plane waves in (11)–(13) were the total fields, the reflecting surface would exhibit locally active-lossy behavior, as was observed in a perfect reflecting metasurface characterization [21].

In this study, we demonstrate lossless surface designs for polarization-preserving reflections. For the surface waves introduced on the same side of the reflecting surface as the incident and reflected waves, an orthogonal polarization is adopted. Additional fields of the same polarization will create complex interference patterns for the total field and power profiles. For example, S_n^{TE} in (17) is a result of interference between the incident and desired reflected waves. If the same TE polarization is chosen for the surface waves to be added, a more complex interference pattern for the Poynting vector on the reflecting surface will result, making satisfaction of (9) at all x a challenging design problem, if not impossible. Exploiting the degree of design freedom provided by an orthogonal polarization for the surface waves helps reduce design complexity.

Hence, towards arriving at (9), we introduce a set of three TM-polarized surface waves, as illustrated in Fig. 2(b). For the i th ($i = 1, 2, 3$) surface wave, let the E and H fields be written as

$$\mathbf{E}^{si} = (\hat{x} j \alpha_i + \hat{y} \beta_i) \frac{\eta H_0^{si}}{k} e^{-\alpha_i y} e^{-j\beta_i x}, \quad (19)$$

$$\mathbf{H}^{si} = \hat{z} H_0^{si} e^{-\alpha_i y} e^{-j\beta_i x}, \quad (20)$$

where $\alpha_i (>0)$ and $\beta_i (>k)$ are the attenuation and propagation constants that satisfy $\alpha_i = \sqrt{\beta_i^2 - k^2}$ and H_0^{si} is the complex amplitude of the i th \hat{z} -polarized magnetic field. The total surface-wave fields are given by superposition as

$(\mathbf{E}^{sw}, \mathbf{H}^{sw}) = (\mathbf{E}^{s1} + \mathbf{E}^{s2} + \mathbf{E}^{s3}, \mathbf{H}^{s1} + \mathbf{H}^{s2} + \mathbf{H}^{s3})$. Here, let the three propagation constants be equally spaced in wave number by $\Delta\beta$, so that $\beta_2 = \beta_1 + \Delta\beta$ and $\beta_3 = \beta_2 + \Delta\beta$. Also, let the amplitudes of the surface waves be written in terms of relative magnitudes b_2, b_3 and relative phases γ_2, γ_3 as

$$H_0^{s2} = b_2 e^{j\gamma_2} H_0^{s1}, \quad H_0^{s3} = b_3 e^{j\gamma_3} H_0^{s1}. \quad (21)$$

Then, the normal component of the Poynting vector for the TM-polarized fields is given by

$$S_n^{\text{TM}} = \frac{\eta |H_0^{s1}|^2}{2k} b \cos(\Delta\beta x + \gamma) - \frac{\eta |H_0^{s1}|^2}{2k} b_3 (\alpha_3 - \alpha_1) \sin(2\Delta\beta x - \gamma_3), \quad (22)$$

where b and γ are the magnitude and phase of the complex number

$$b e^{j\gamma} = b_2 \{[(\alpha_2 - \alpha_1) \sin \gamma_2 - b_3 (\alpha_3 - \alpha_2) \sin(\gamma_2 - \gamma_3)] + j[(\alpha_2 - \alpha_1) \cos \gamma_2 + b_3 (\alpha_3 - \alpha_2) \cos(\gamma_2 - \gamma_3)]\}. \quad (23)$$

Since TE- and TM-polarized fields are orthogonal, their power densities add algebraically, giving the normal component of the Poynting vector of the total fields as $S_n = S_n^{\text{TE}} + S_n^{\text{TM}}$.

It is desired that the TM-mode surface waves be designed to produce a globally lossless and reciprocal surface by enforcing (9) for all x . Three complex amplitudes H_0^{si} ($i = 1, 2, 3$) and two real-valued parameters $\beta_1, \Delta\beta$ uniquely determine the surface waves. First, the wave numbers along the x -axis direction for two sets of spatial sinusoidal functions in S_n^{TE} and S_n^{TM} must match, so we require

$$\Delta\beta = k_x^r. \quad (24)$$

The remaining conditions on the sinusoidal functions with wave numbers k_x^r and $2k_x^r$ in (17) and (22) for canceling each other and giving $S_n = 0$ are

$$\frac{\eta |H_0^{s1}|^2}{2k} b = \frac{a |E_0^i|^2}{2} \left(\frac{1}{Z_i} - \frac{1}{Z_r} \right), \quad (25)$$

$$\gamma = \delta, \quad (26)$$

$$\frac{\eta |H_0^{s1}|^2}{2k} b_3 (\alpha_3 - \alpha_1) = \frac{a_1 a_2 |E_0^i|^2}{Z_r}, \quad (27)$$

$$\gamma_3 = \delta_2 - \delta_1 - \frac{\pi}{2}. \quad (28)$$

The solution for three surface waves that satisfy these conditions is not unique. Here, we present one set of solutions. The phase of H_0^{s1} does not enter into (9), so it can be assigned an arbitrary value. Next, we choose to set the propagation constant β_1 of \mathbf{H}^{s1} to a value in the allowed range $\beta_1 > k$. The remaining propagation constants β_2, β_3 and all three attenuation constants α_i ($i = 1, 2, 3$) are now determined. At this point, there are four equations [(25)–(28)] for five unknowns ($|H_0^{s1}|, b_2, b_3, \gamma_2$, and γ_3). Out of these five, let us pick $|H_0^{s1}|$ to some value. Then, the values of b_3 and γ_3 are determined from (27) and (28), respectively. In terms of b and γ obtained using (25) and (26), the relation between b_2 and γ_2

can be found from (23) in a matrix form as

$$\begin{bmatrix} \sin \gamma_2 \\ \cos \gamma_2 \end{bmatrix} = \frac{b}{b_2[(\alpha_2 - \alpha_1)^2 - b_3^2(\alpha_3 - \alpha_2)^2]} \begin{bmatrix} \alpha_2 - \alpha_1 + b_3(\alpha_3 - \alpha_2) \cos \gamma_3 & -b_3(\alpha_3 - \alpha_2) \sin \gamma_3 \\ -b_3(\alpha_3 - \alpha_2) \sin \gamma_3 & \alpha_2 - \alpha_1 - b_3(\alpha_3 - \alpha_2) \cos \gamma_3 \end{bmatrix} \begin{bmatrix} \cos \gamma \\ \sin \gamma \end{bmatrix}. \quad (29)$$

The value of b_2 is determined by enforcing $\sin^2 \gamma_2 + \cos^2 \gamma_2 = 1$. The phase angle γ_2 is subsequently found from (29).

IV. DESIGN EXAMPLES

A. Perfect anomalous reflector

Reflecting metasurfaces for achieving high power-conversion efficiencies for anomalous reflection beyond the theoretical limits associated with the generalized law of reflection are being actively investigated. Using a strongly nonlocal metasurface based on the leaky-wave radiation principle, a 94% reflection power-conversion efficiency was experimentally achieved for 0° -to- 70° reflection [12]. In [24], the theoretical design for a free-standing Ω -bianisotropic metasurface was reported. Here, a perfect anomalous reflection is designed for an impenetrable surface in terms of the anisotropic surface impedance and is numerically validated.

An anomalous reflection with angles from 0 to $+\theta^r$ measured from the $+y$ axis can be treated as a special case of Fig. 2(b) with $a_1 = 0$. The power-conservation condition (14) gives

$$a_2 = \sqrt{\frac{Z_r}{Z_i}} = \sqrt{\frac{1}{\cos \theta^r}}, \quad (30)$$

which is larger than unity. Hence, the reflected E field has a larger magnitude than the incident E field. This occurs when the angle of incidence is smaller than the angle of reflection. The values of a and δ are found from (18) to be

$$a = a_2, \quad \delta = -\delta_2. \quad (31)$$

Only two surface waves are needed for the total fields to satisfy (9). As was the case for the three-channel controller design in Sec. III, the design for the surface waves \mathbf{H}^{s1} and \mathbf{H}^{s2} is not unique. Specifically, only two equations, (25) and (26), need to be enforced for four real-valued parameters: the magnitude and phase of H_0^{s1} , b_2 , and γ_2 . Let us set the magnitude and phase of H_0^{s1} to some chosen values. Then, the parameter b is found from (25). Finally, the remaining two design parameters are found from (29) to be

$$b_2 = \frac{b}{\alpha_2 - \alpha_1}, \quad \gamma_2 = \frac{\pi}{2} - \gamma. \quad (32)$$

As an example, let us consider a perfect in-phase reflection ($\delta_2 = 0$) to $\theta^r = 70^\circ$ for normal incidence with an electric field of unit amplitude ($E_0^i = 1$ V/m). This reflection angle gives the tangential wave number for the reflected plane wave to be $k_x^r = k \sin 70^\circ = 0.940k$. While β_1 can be chosen to be an arbitrary value in the invisible region ($\beta_1 > k$), let us choose the minimum integer multiple of k_x^r so that the surface waves and, as a consequence, the surface-impedance parameters become periodic in x with a period $D_x = 1.064\lambda$ for demonstration purposes, as are the TE-mode propagating fields (11)–(13). Hence, we have $\beta_1 = 2k_x^r = 1.879k$ and $\Delta\beta = k_x^r = 0.940k$.

Next, we select $H_0^{s1} = |E_0^i| \sqrt{ka(1/Z_i - 1/Z_r)/(\alpha_2 - \alpha_1)\eta} = 2.753$ mA/m. This value was chosen to give $b_2 = 1$, i.e., to set the H -field magnitudes of the two surface waves equal to each other. Finally, the phase angle of H_0^{s2} is found to be $\gamma_2 = \pi/2$ from (26), (31), and (32).

Figure 3(a) shows the normal component of the time-average Poynting vector for the TE-polarized propagating and TM-polarized evanescent waves, $S_n^{\text{TE}}(x)$ and $S_n^{\text{TM}}(x)$. Each is a single sinusoidal function with a period of D_x having a net value of zero over the period. The two surface waves were designed such that S_n^{TM} has the same magnitude but is 180° out of phase with S_n^{TE} , so that the two add to nullify each other. As indicated in Fig. 3(a), the net negative power associated with $S_n^{\text{TE}}(x) < 0$ is converted into the TM mode in $|x| < D_x/4 = 0.266\lambda$. The surface waves carry this power along the surface, which remains closely bound to the interface. In the range where $S_n^{\text{TM}}(x) < 0$, this TM-mode power is converted back into the TE mode and launched into

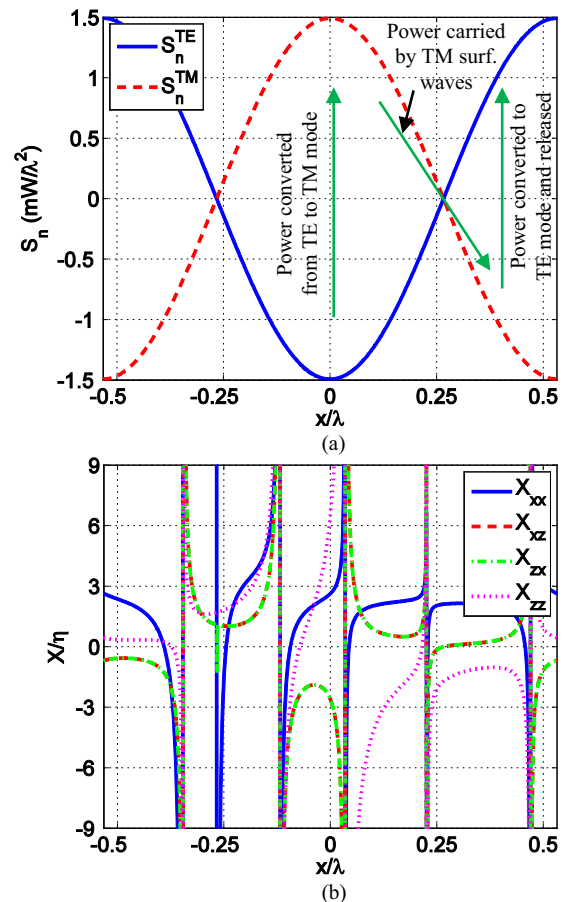


FIG. 3. Characteristics of a 0° -to- 70° perfect anomalous reflecting surface. (a) The normal component of the Poynting vector of TE-mode propagating and TM-mode surface waves. (b) The elements of the surface reactance tensor \mathbf{X}_s .

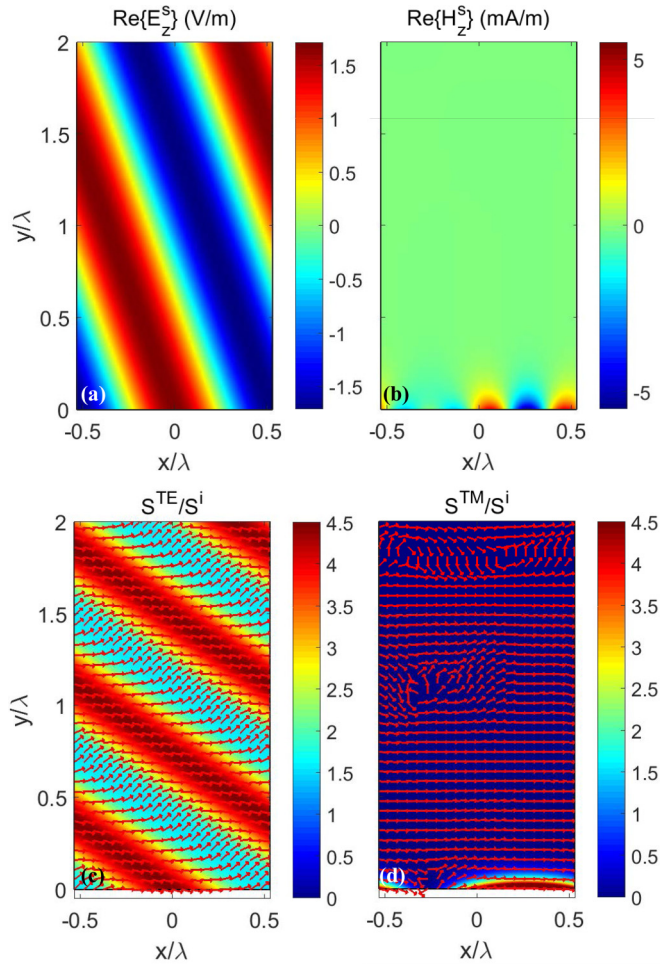


FIG. 4. Simulated performance of the 0° -to- 70° perfect anomalous reflector. (a) Snapshot of the scattered TE-mode electric field E_z^s . (b) Snapshot of the scattered TM-mode magnetic field H_z^s . (c) Poynting vector and its magnitude of the TE-mode fields. (d) Poynting vector and its magnitude of the TM-mode fields. The Poynting vector magnitudes are normalized by the power density of the incident plane wave. The incident E -field amplitude is $E_0^i = 1$ V/m.

free space as a propagating plane wave in the anomalous direction. The four elements of the surface reactance tensor \mathbf{X}_s in (5) are plotted in Fig. 3(b). They are evaluated using (7) from the complete field description. Each element is a periodic function with the same period D_x . The off-diagonal elements are equal to each other ($X_{xz} = X_{zx}$) as designed, making the reflecting surface pointwise lossless and reciprocal everywhere. It is noted that all four reactance element values range from $-\infty$ to $+\infty$. The rapid spatial variation over the period of $D_x = 1.064\lambda$ (e.g., X_{xx} diverges to $-\infty$ six times) is related to the choice of $\beta_1 = 1.879k$. It will become less rapid when β_1 is set closer to k .

The performance of the reflecting surface design is numerically analyzed using COMSOL MULTIPHYSICS, and the results are shown in Fig. 4. The E -field amplitude of the normally incident plane wave is $E_0^i = 1$ V/m. Figure 4(a) shows a snapshot of the z component of the scattered E field $\text{Re}\{E_z^s\}$ over the range $-D_x/2 < x < D_x/2$ and $0 < y < 2\lambda$.

A pure plane wave propagating in $\theta^r = 70^\circ$ is observed with a correctly amplified E -field magnitude of 1.71 (note that power is conserved, not amplified). The reflected TE-mode field is an unperturbed reflected plane-wave field all the way down to the reflector surface. This contrasts with the presence of surface waves of the same polarization near the surface in the perfect reflector design based on the leaky-wave principle [12]. A snapshot of the z component of the TM-mode surface wave $\text{Re}\{H_z^s\}$ is plotted in Fig. 4(b). As designed, the TM-mode fields are tightly bound to the surface and as a result do not affect the specified far-field reflection characteristics. The vector and magnitude of the Poynting vectors for the TE- and TM-mode fields are shown in Figs. 4(c) and 4(d), respectively. The magnitude is normalized by the power density of the incident field $S^i = |E_0^i|^2/2\eta$. An interference pattern between the incident and reflected plane waves is evident in Fig. 4(c). At $y = 0$, the arrows representing the time-average Poynting vector penetrate the reflecting plane, but its normal component is canceled by that of the TM-mode fields shown in Fig. 4(d) along the x axis. The TM-mode Poynting vector shows an interference pattern between two surface waves, with the power density quickly reducing toward zero away from the surface. The maximum relative magnitude of the TM-mode Poynting vector is found to be 10.1, while that of the TE-mode fields is 4.50. The direction of TM-mode power flow is along the $+x$ axis because of the positive sign choices for β_1 and β_2 . The simulated S -parameter results show perfect performance of anomalous reflection with zero back-reflection, $S_{13} = S_{33} = 0$ and $S_{23} = 1 \angle 0$, as designed, where the phase is referenced at $y = 0$.

B. Power splitter with 1:9 power division

Next, an example design of a plane-wave power splitter in the $\pm 70^\circ$ directions with an unequal power division ratio of 1:9 with zero back-reflection is considered. To illustrate the robustness of the design, let us make arbitrary choices of 20° and 50° for the two reflection phases such that

$$a_1 e^{j\delta_1} = 0.541 e^{j0.349}, \quad a_2 e^{j\delta_2} = 1.622 e^{j0.873}, \quad (33)$$

where the values of a_1 , a_2 are found using the power-conservation relation (14) for a lossless surface. The associated values of a and δ are found from (18) to be $a = 1.877$ and $\delta = -0.599$ rad. As explained in Sec. III, both the magnitude and phase of H_0^{s1} can be set to arbitrary values. We choose to pick

$$H_0^{s1} = \frac{|E_0^i|}{\eta} \sqrt{\frac{k}{\beta_1}}. \quad (34)$$

This is based on the condition that the tangential component of the Poynting vector associated with \mathbf{H}^{s1} on the surface is equal to the power density of the illuminating plane wave, i.e., $\eta\beta_1 |H_0^{s1}|^2/2k = S^i$. In addition, a zero phase angle is selected. For a unit-amplitude incident E field ($E_0^i = 1$ V/m), this amounts to $H_0^{s1} = 1.935$ mA/m. Here, the propagation constants of the surface waves are selected to be the same as those in Sec. IV A, $\beta_1 = 2k_x^r = 1.879k$ and $\Delta\beta = k_x^r = 0.940k$. From (27) and (28), it is found that $b_3 = 0.555$ and $\gamma_3 = -1.047$ rad. Using $be^{j\gamma} = 14.59e^{-j0.599}$ given by (23),

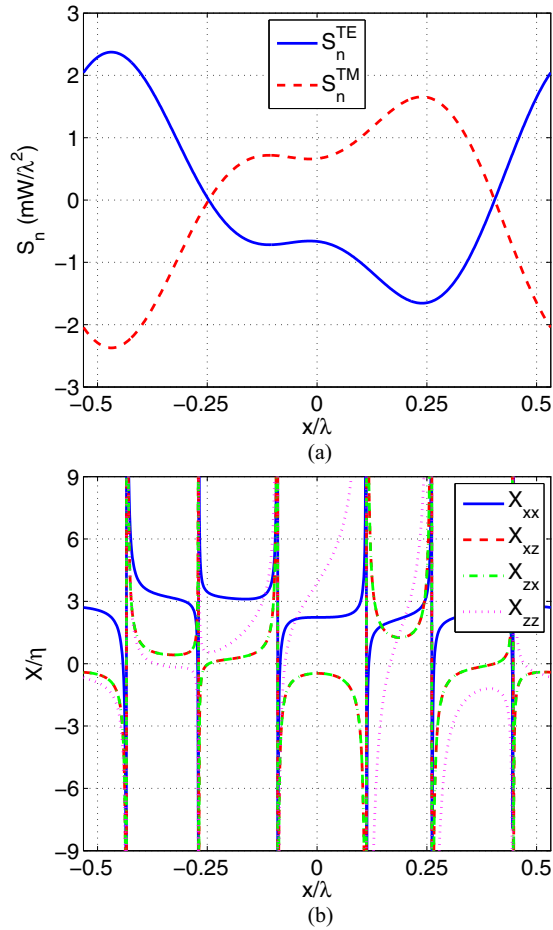


FIG. 5. Properties of a 1:9 power splitter of a normally incident plane wave into $\theta^r = \pm 70^\circ$. (a) The normal component of the Poynting vector for the TE-polarized propagating and TM-polarized surface waves. (b) The four elements of a reactance tensor \mathbf{X}_s normalized by the free-space intrinsic impedance η .

the remaining two parameters for complete specification of the surface waves are found to be $b_2 = 2.415$ and $\gamma_2 = 1.622$ rad.

Over a single period of $D_x = 1.064\lambda$, the normal components of the Poynting vector for the TE- and TM-mode fields are plotted in Fig. 5(a). Each is a superposition of two sinusoidal functions with periods $D_x/2$ and D_x . As intended, the two Poynting vector components cancel each other, and (9) is satisfied as a result, producing a lossless and reciprocal tensor surface impedance. This is confirmed in Fig. 5(b), where the four reactance tensor elements calculated using (7) are shown. The off-diagonal terms X_{xz} and X_{zx} are identical to each other. All four tensor elements are highly inhomogeneous.

The splitter design was simulated using COMSOL MULTIPHYSICS. The predicted performance of the 1:9 power splitter with an incident E -field amplitude of $E_0^i = 1$ V/m is shown in Fig. 6. A snapshot of the z component of the scattered TE-mode E field E_z^s is plotted in Fig. 6(a). Unlike in the perfect reflector design, the presence of more than one plane wave is evident. Figure 6(b) shows a snapshot of the z component of the scattered magnetic field H_z^s . The TM-mode surface-wave fields are tightly bound to the surface and do not reach the far zone. The time-average Poynting vector for the TE-mode fields

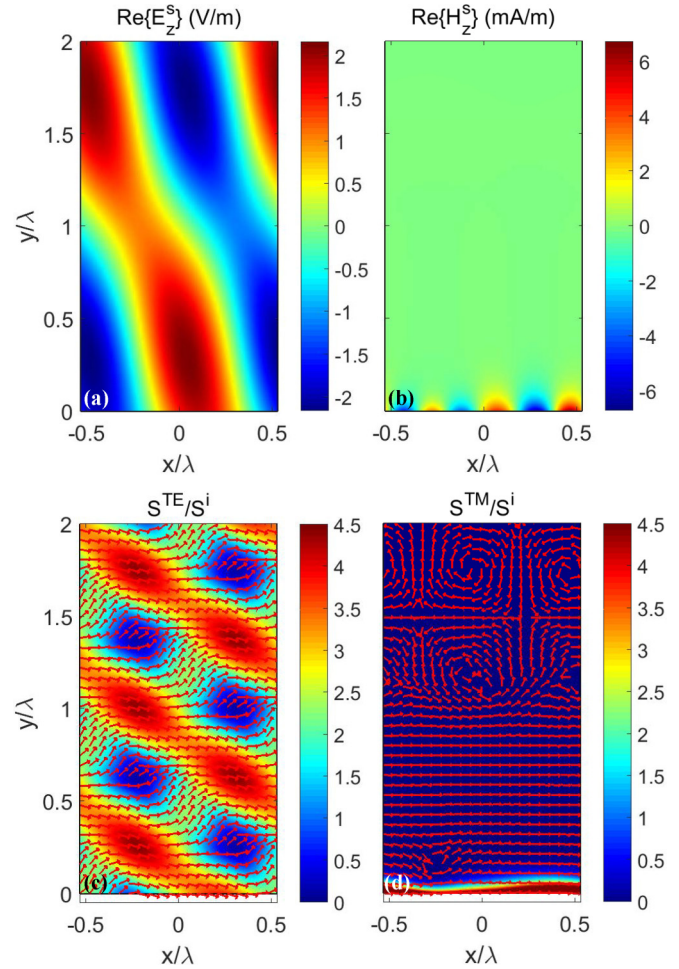


FIG. 6. Simulated performance of the 1:9 power splitter. (a) A snapshot of the scattered TE-mode electric field component E_z^s . (b) A snapshot of the scattered TM-mode surface-wave field component H_z^s . (c) The vector and magnitude of the TE-mode Poynting vector. (d) The vector and magnitude of the TM-mode Poynting vector. The amplitude of the incident E field is $E_0^i = 1$ V/m.

is plotted in Fig. 6(c). On the reflecting surface at $y = 0$, the profile of the normal Poynting vector component of the total TE-mode fields agrees with the designed variation in Fig. 5(a). It is canceled by the normal component of the TM-mode Poynting vector along $y = 0$, shown in Fig. 6(d). The highest value of the normalized magnitude of the TM-mode Poynting vector in Fig. 6(d) is found to be 17.9, while the highest value for the TE mode is 4.43. The surface waves carry power in the $+x$ -axis direction from the x range where $S_n^{\text{TE}}(x) < 0$ to where $S_n^{\text{TE}}(x) > 0$. Unlike in the perfect reflector design in Sec. IV A, some of the power channeled by the surface waves is launched backward, in the direction of $\theta^r = -70^\circ$. The simulated S -parameter results are $S_{13} = 0.316\angle 20.0^\circ$, $S_{23} = 0.949\angle 50.0^\circ$, and $S_{33} = 0$. They agree with the desired characteristics in both magnitude ($|S_{13}|^2 : |S_{23}|^2 : |S_{33}|^2 = 0.1 : 0.9 : 0$) and phase.

V. REALIZATION PROSPECTS

A lossless and reciprocal surface impedance allows an accurate realization as a passive metasurface using the standard

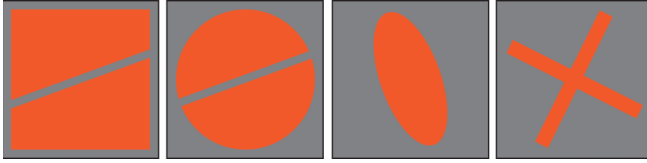


FIG. 7. Illustration of different conductor patch shapes on a grounded dielectric substrate for realizing an anisotropic tensor surface reactance. The solid gray square indicates the unit cell and the dielectric substrate. The conductor patch is shown in brown.

printed-circuit technologies. A symmetric reactance tensor \mathbf{X}_s in (7) is diagonalized using two real-valued eigenvalues and two orthogonal eigenvectors in the xz plane, which are the principal values and directions associated with surface reactance synthesis. For an impenetrable surface, one or more layers of planar arrays of conductor patches on a grounded dielectric substrate are a candidate physical configuration. A variety of conductor patch unit cells for realizing tensor or anisotropic surface reactance parameters has been reported in the literature [29–31]. Examples of potential conductor patch resonator geometry are illustrated in Fig. 7.

In Sec. IV, the wave number β_1 of \mathbf{H}^{s1} was chosen to be $\beta_1 = 2k_x^r = 1.879k$ in order to make the total fields, and as a result the surface parameters have a period of D_x . This rather large value of β_1 contributes to the highly spatially inhomogeneous reactance parameters in Figs. 3(b) and 5(b). As previously mentioned, a smaller value of β_1 that is closer to k helps alleviate the resulting spatial inhomogeneity. To illustrate this point, a propagation constant of $\beta_1 = 1.034k$ is considered here for the 0° -to- 70° design presented in Sec. IV A. Here, β_1 is determined from the chosen relation $\beta_1 = (11/10)k_x^r$, and this makes the surface waves ($\mathbf{E}^{s1}, \mathbf{H}^{s1}$) and ($\mathbf{E}^{s2}, \mathbf{H}^{s2}$) periodic with a period of $10D_x = 10.64\lambda$. For the associated lossless, reciprocal anomalous reflector design, the two principal values of the reactance tensor \mathbf{X}_s , obtained through diagonalization are plotted in Fig. 8(a) as solid curves. They are associated with two orthogonal principal directions, which are given by the eigenvectors of \mathbf{X}_s (not shown). The solid blue and green curves indicate the larger and smaller values of the two principal values, respectively. One of the two principal reactances becomes infinite in magnitude at three locations, $x/\lambda \approx 0.046, 0.382,$ and 0.802 , within the single wavelength range shown, corresponding to the magnetic-wall resonance (i.e., an artificial magnetic conductor condition). A typical metasurface realization samples the required surface reactances at a fixed subwavelength interval. If we choose to assign four spatial sampling points to an x interval bounded by diverging reactances, it is anticipated that an approximate meta-atom dimension of $\lambda/10$ is needed to represent the highly inhomogeneous tensor reactance profile.

In order to qualitatively assess the effect of the aforementioned discretization or sampling of the ideal surface parameters in practical realizations, anomalous reflection performance using a piecewise-constant (i.e., staircase) reactance profile is simulated. The discretized principal reactance values with a sampling interval of $\lambda/10$ are shown in Fig. 8(a) as dashed curves. Over a supercell period of 10.64λ , Figs. 8(b) and 8(c) show snapshots of the scattered E - and H -field

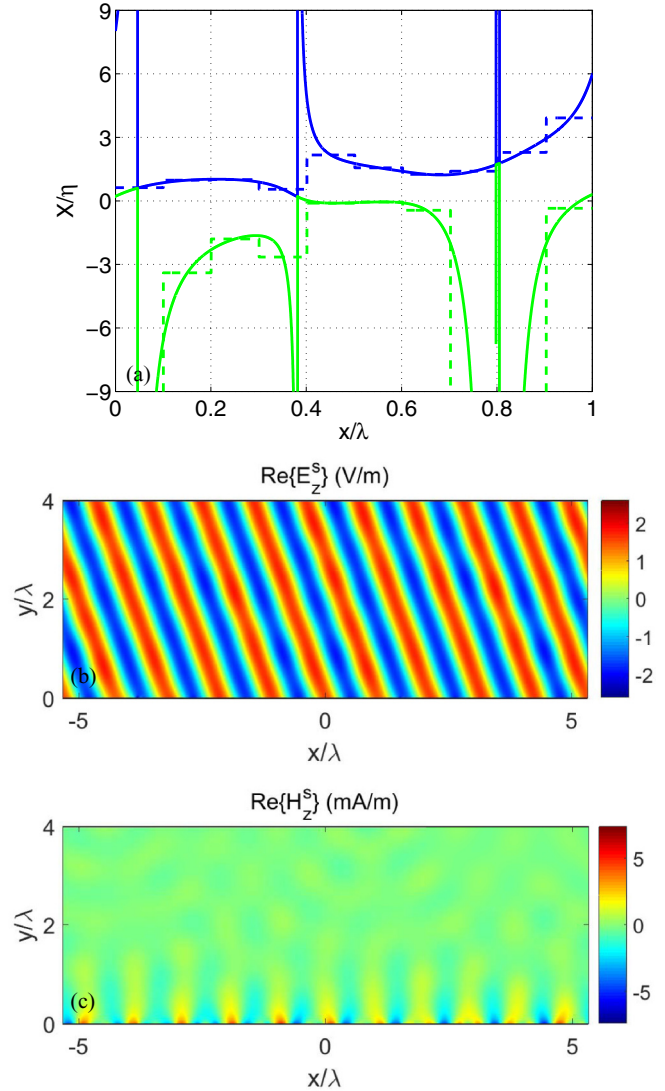


FIG. 8. Characteristics of an anomalous reflector surface with piecewise-constant surface-impedance parameters. (a) The two principal values of \mathbf{X}_s for the perfect anomalous reflector in Sec. IV A with a choice $\beta_1 = 1.034k$. The solid blue and green lines indicate higher and lower values, respectively. For each principal reactance, the associated discretized values are shown as dashed lines. (b) A snapshot of the scattered TE-mode electric field E_z^s . (c) A snapshot of the scattered TM-mode magnetic field H_z^s .

components. Deterioration of the reflected wave from a pure $+70^\circ$ -propagating plane wave is visible in Fig. 8(b), but the degradation is minor. The simulated S -parameter values are $S_{13} = 0.033 \angle -153.1^\circ$, $S_{23} = 0.995 \angle 1.71^\circ$, and $S_{33} = 0.019 \angle -56.1^\circ$, which are close to the ideal values. These correspond to a power reflection efficiency into the anomalous direction of 99.0% and a back-reflection of 0.04%. The remaining power is scattered in multiple diffraction orders associated with the supercell period. An evanescent TM-polarized wave is visible in Fig. 8(c). Hence, even with unavoidable discretization of the highly inhomogeneous tensor surface impedance in practice, the performance of a metasurface that is properly designed and implemented may closely approach that of the ideal design.

VI. CONCLUSION

For an impenetrable reflecting interface, the exact tensor impedance boundary condition was derived for realizing a desired reflection transformation under a given propagating-wave illumination. With the total fields specified by a superposition of the incident fields and the desired reflected fields, application of the standard impedance boundary condition typically leads to spatially dispersive active-lossy profiles. By introducing a set of carefully chosen surface waves of orthogonal polarization, the surface impedance can be made pointwise lossless and reciprocal by channeling the necessary power along the surface. The orthogonal polarization for the surface waves not only avoids interference with the propagating

waves but also allows both the propagating and surface waves to coexist on the same side of the reflecting surface.

The proposed surface-impedance design allows realization of a perfect reflecting surface as an impenetrable metasurface of subwavelength thickness. An array of subwavelength conductor patches on a grounded dielectric substrate is a prime candidate configuration for metasurface realization at microwave frequencies. Since the degree of spatial variation of reactance parameters depends on the propagation constants of the surface waves, it is advantageous to select them to be low at values just outside the visible range. Thin metasurface realizations of the proposed reflection transformers are currently under investigation.

-
- [1] C. L. Holloway, E. F. Kuester, J. A. Gordon, J. O'Hara, J. Booth, and D. R. Smith, An overview of the theory and applications of metasurfaces: The two-dimensional equivalents of metamaterials, *IEEE Antennas Propag. Mag.* **54**, 10 (2012).
- [2] N. Yu and F. Capasso, Flat optics with designer metasurfaces, *Nat. Mater.* **13**, 139 (2014).
- [3] S. A. Tretyakov, Metasurfaces for general transformations of electromagnetic fields, *Philos. Trans. R. Soc. A* **373**, 20140362 (2015).
- [4] S. B. Glybovski, S. A. Tretyakov, P. A. Belov, Y. S. Kivshar, and C. R. Simovski, Metasurfaces: From microwaves to visible, *Phys. Rep.* **634**, 1 (2016).
- [5] N. I. Landy, S. Sajuyigbe, J. J. Mock, D. R. Smith, and W. J. Padilla, Perfect Metamaterial Absorber, *Phys. Rev. Lett.* **100**, 207402 (2008).
- [6] Y. Ra'di, V. S. Asadchy, and S. A. Tretyakov, Total absorption of electromagnetic waves in ultimately thin layers, *IEEE Trans. Antennas Propag.* **61**, 4606 (2013).
- [7] V. S. Asadchy, Y. Ra'di, J. Vehmas, and S. A. Tretyakov, Functional Metamirrors Using Bianisotropic Elements, *Phys. Rev. Lett.* **114**, 095503 (2015).
- [8] T. Niemi, A. O. Karilainen, and S. A. Tretyakov, Synthesis of polarization transformers, *IEEE Trans. Antennas Propag.* **61**, 3102 (2013).
- [9] N. Yu, P. Genevet, M. A. Kats, F. Aieta, J.-P. Tetienne, F. Capasso, and Z. Gaburro, Light propagation with phase discontinuities: Generalized laws of reflection and refraction, *Science* **334**, 333 (2011).
- [10] S. Sun, K.-Y. Yang, C.-M. Wang, T.-K. Juan, W. T. Chen, C. Y. Liao, Q. He, S. Xiao, W.-T. Kung, G.-Y. Guo, L. Zhou, and D. P. Tsai, High-efficiency broadband anomalous reflection by gradient metasurfaces, *Nano Lett.* **12**, 6223 (2012).
- [11] Z. Li, E. Palacios, S. Butun, and K. Aydin, Visible-frequency metasurfaces for broadband anomalous reflection and high-efficiency spectrum splitting, *Nano Lett.* **15**, 1615 (2015).
- [12] A. Díaz-Rubio, V. S. Asadchy, A. Elsakka, and S. A. Tretyakov, From the generalized reflection law to the realization of perfect anomalous reflectors, *Sci. Adv.* **3**, e1602714 (2017).
- [13] D. Lin, P. Fan, E. Hasman, and M. L. Brongersma, Dielectric gradient metasurface optical elements, *Science* **345**, 298 (2014).
- [14] Q. Wang, X. Zhang, Y. Xu, Z. Tian, J. Gu, W. Yue, S. Zhang, J. Han, and W. Zhang, A broadband metasurface-based terahertz flat-lens array, *Adv. Opt. Mater.* **3**, 779 (2015).
- [15] M. Khorasaninejad, W. T. Chen, R. C. Devlin, J. Oh, A. Y. Zhu, and F. Capasso, Metalenses at visible wavelengths: Diffraction-limited focusing and subwavelength resolution imaging, *Science* **362**, 1190 (2016).
- [16] X. Ni, A. V. Kildishev, and V. M. Shalaev, Metasurface holograms for visible light, *Nat. Commun.* **4**, 2087 (2013).
- [17] G. Zheng, H. Mühlenbernd, M. Kenney, G. Li, T. Zentgraf, and S. Zhang, Metasurface holograms reaching 80% efficiency, *Nat. Nanotechnol.* **10**, 308 (2015).
- [18] P. Genevet and F. Capasso, Holographic optical metasurfaces: A review of current progress, *Rep. Prog. Phys.* **78**, 024401 (2015).
- [19] C. Pfeiffer and A. Grbic, Metamaterial Huygens' Surfaces: Tailoring Wave Fronts with Reflectionless Sheets, *Phys. Rev. Lett.* **110**, 197401 (2013).
- [20] J. Huang and J. A. Encinar, *Reflectarray Antennas* (Wiley-IEEE Press, Hoboken, NJ, 2008).
- [21] V. S. Asadchy, M. Albooyeh, S. N. Tcvetkova, A. Díaz-Rubio, Y. Ra'di, and S. A. Tretyakov, Perfect control of reflection and refraction using spatially dispersive metasurfaces, *Phys. Rev. B* **94**, 075142 (2016).
- [22] N. Mohammadi Estakhri and A. Alù, Wave-Front Transformation with Gradient Metasurfaces, *Phys. Rev. X* **6**, 041008 (2016).
- [23] A. Epstein and G. V. Eleftheriades, Arbitrary power-conserving field transformations with passive lossless Omega-type bianisotropic metasurfaces, *IEEE Trans. Antennas Propag.* **64**, 3880 (2016).
- [24] A. Epstein and G. V. Eleftheriades, Synthesis of Passive Lossless Metasurfaces Using Auxiliary Fields for Reflectionless Beam Splitting and Perfect Reflection, *Phys. Rev. Lett.* **117**, 256103 (2016).
- [25] A. Epstein and G. V. Eleftheriades, Shielded perfect reflectors based on omega-bianisotropic metasurfaces, *International Workshop on Antenna Technology: Small Antennas, Innovative Structures, and Applications (iWAT)* (IEEE, Athens, 2017).
- [26] R. F. Harrington, *Time-Harmonic Electromagnetic Fields* (Wiley-IEEE Press, Hoboken, NJ, 2001).
- [27] V. S. Asadchy, A. Díaz-Rubio, S. N. Tcvetkova, D.-H. Kwon, A. Elsakka, M. Albooyeh, and S. A. Tretyakov, Flat Engineered Multi-Channel Reflectors, [arXiv:1610.04780](https://arxiv.org/abs/1610.04780).

- [28] If a desired set of reflection angles θ_m^r ($m = 0, \pm 1, \pm 2, \dots$) in the visible region is not related via (10) with some period D_x , the surface parameters are not periodic functions.
- [29] B. H. Fong, J. S. Colburn, J. J. Ottusch, J. L. Visher, and D. F. Sievenpiper, Scalar and tensor holographic artificial impedance surfaces, *IEEE Trans. Antennas Propag.* **58**, 3212 (2010).
- [30] G. Minatti, S. Maci, P. D. Vita, A. Freni, and M. Sabbadini, A circularly-polarized isoflux antenna based on anisotropic metasurface, *IEEE Trans. Antennas Propag.* **60**, 4998 (2012).
- [31] A. M. Patel and A. Grbic, Modeling and analysis of printed-circuit tensor impedance surfaces, *IEEE Trans. Antennas Propag.* **61**, 211 (2013).